NATIONAL ADVISORY COMMITTEE FOR AERONAUTICS

WARTIME REPORT

ORIGINALLY ISSUED
March 1943 as
Advance Confidential Report

AIR-FLOW SURVEYS IN THE REGION OF THE TAIL SURFACES OF A SINGLE-ENGINE AIRPLANE EQUIPPED WITH DUAL-ROTATING PROPELLERS

By Harold H. Sweberg

Langley Memorial Aeronautical Laboratory
Langley Field, Va.

NACA

WASHINGTON

NATIONAL ADVISORY COMMITTEE FOR AERONAUTICS

ADVANCE CONFIDENTIAL REPORT

AIR-FLOW SURVEYS IN THE REGION OF THE TAIL SURFACES OF A SINGLE-ENGINE AIRPLANE EQUIPPED WITH DUAL-ROTATING PROPELLERS

By Harold H. Sweberg

SUMMARY

Surveys of the air flow in the region of the tail surfaces of a single-engine pursuit-type airplane equipped with dual-rotating propellers are presented. The tests included air-flow measurements with propellers removed and oporating at various thrust coefficients and with flaps retracted and deflected. Some comparisons are made with air-flow measurements at the tail of a model equipped with a single-rotating propeller. The tests were made in the NACA full-scale tunnel.

INTRODUCTION

As part of a general investigation directed toward predicting the effects of propeller operation on the stability characteristics of aircraft, measurements were made of the air flow in the region of the tail surfaces of a single-engine pursuit-type airplane equipped with dual-rotating propellers. The tests were made in the NACA full-scale tunnel and included air-flow measurements with propellers removed and operating and with landing flaps deflected 40° and retracted.

Investigations of the air flow in the region of the tail surfaces of airplanes equipped with single-rotating propellers have also been made and are reported in references 1 and 2. Some comparisons are given in this paper of the air flow behind single- and dual-rotating propellers.

SYMBOLS

C_L lift coefficient

T_c thrust coefficient $\left(\frac{\text{effective thrust}}{\rho V^2 D^2}\right)$

C_P power coefficient $\left(\frac{\text{engine power}}{\rho n^3 D^5}\right)$

V/nD propeller advance–diameter ratio

η propeller efficiency

V airspeed

n propeller rotational speed

D propeller diameter

ρ density of air

α_T angle of attack of thrust axis relative to free–stream direction, degrees

β propeller blade angle; subscripts F and R refer to front and rear propellers

ϵ local downwash angle at tail measured relative to free–stream direction

ϵ_{av} average downwash angle across elevator hinge line as found from air–flow surveys

$\Delta\epsilon$ angular difference between average downwash angles across semispans of horizontal tail surface

q local dynamic pressure

q_o free–stream dynamic pressure

$(q/q_o)_{av}$ average dynamic–pressure ratio across elevator hinge line as found from air–flow surveys

DESCRIPTION OF MODEL AND TESTS

The NACA full-scale tunnel is described in reference 3 and the methods by which the data were corrected for jet-boundary and blocking effects are discussed in references 4 and 5.

The model mounted on the tunnel supports is shown in figure 1. Figure 2 is a three-view drawing showing the important dimensions of the model. The outer surfaces of the model were constructed of sheet aluminum that was covered with a plastic filler and sanded to a smooth finish before the tests were made. The horizontal and vertical tail surfaces were removed for all the tests. Balanced slotted flaps, having a flap span equal to 54 percent of the wing span, were used as the high-lift device.

The propulsive unit consisted of two 10-foot-diameter dual-rotating propellers that were driven by two 25-horsepower electric motors installed in the fuselage. The front motor was directly connected to the front propeller, while the rear motor drove the rear propeller through chains and a countershaft.

The propeller installation on the model is shown in figure 3. The blade-angle setting of the front propeller was 28.0°. In order that the rear propeller absorb the same amount of power at peak efficiency as the front propeller, the blade-angle setting of the rear propeller was 27.7°. The blade angle of the rear propeller was set lower than that of the front propeller to offset its increased angle of attack due to the introduction of a rotational component to the slipstream by the front propeller. The propeller blade angles were held constant for the tests. The aerodynamic characteristics of the dual-rotating propellers on the complete model at about zero lift coefficient are shown in figure 4.

All the surveys were made in a vertical plane through the elevator hinge line. The surveys were made at various angles of attack with propellers removed and operating and with landing flaps deflected 40° and retracted.

The measurements were made with a rack of fifteen 3/8-inch steel survey tubes described in reference 2. The accuracy of the pitch- and yaw-angle measurements is estimated to be within about ±0.25°; dynamic-pressure measurements are accurate within about ±1 percent.

RESULTS AND DISCUSSION

The air-flow surveys are presented as contours of dynamic-pressure ratio q/q_o and as vectors showing the resultant flow direction in a vertical plane through the elevator hinge line. The results of the propellers-removed tests, which are given as a reference for the determination of the slipstream effects, are shown in figures 5 and 6. Figures 7 and 8 give the results of the tests with propellers operating at various thrust coefficients for flaps retracted and for flaps deflected 40°, respectively.

The effects of propeller operation on the average dynamic pressures and the average downwash angles at the tail are illustrated in table I. The dynamic-pressure ratios and the downwash angles were not weighted according to the variation of local chord and local dynamic pressure across the tail span, inasmuch as a few computations showed this correction to be small. The values of $(q/q_o)_{av}$ and ϵ_{av} have been computed separately across each semispan of the horizontal tail surface in order to ascertain whether the use of dual-rotating propellers eliminated the effects due to slipstream rotation.

When the power absorbed by the front propeller was approximately equal to the power absorbed by the rear propeller, there was little evidence of slipstream rotation in the surveys. (See figs. 7 and 8.) Because the propeller blade angles were adjusted to absorb approximately equal power at the V/nD for peak efficiency, V/nD = 1.25, the powers absorbed by the two propellers were not equal at other values of V/nD (fig. 4). At low thrust coefficients, for which the differences in the powers absorbed by the front and the rear propellers were small, the values of $(q/q_o)_{av}$ and ϵ_{av} measured across each semispan of the horizontal tail surface were approximately equal. At the higher thrust coefficients, however, some differences in $(q/q_o)_{av}$ and ϵ_{av} were measured, although the differences were considerably less than those usually observed behind airplanes with single-rotating propellers.

In order to compare the air flow behind installations of single- and dual-rotating propellers, some of the results of downwash-angle measurements at the tail of a single-engine pursuit-type airplane equipped with a single-

rotating propeller, which have been reported in reference 1, are given in figures 9 and 10. These figures show the downwash-angle distribution across the horizontal tail span of the model with flaps retracted and with flaps deflected 40° for various angles of attack and various thrust coefficients. Similar curves are given in figures 11 and 12 for the model with dual-rotating propellers.

For the model with the single-rotating propeller and flaps retracted, the original direction of rotation of the slipstream is retained to a large extent at the tail - that is, the downwash angles at the tail on the side of the downgoing blades are increased; whereas the downwash angles at the tail on the side of the upgoing blades are decreased. The slipstream rotation appears to be considerably less at the tail with flaps deflected than with flaps retracted. It appears likely that, with the flaps deflected, the slipstream is deflected below the elevator hinge line with the result that the slipstream rotation affects the resultant downwash-angle distribution across the horizontal tail surface less with flaps deflected than with flaps retracted.

A comparison is given in figure 13 of the angular differences between the average downwash angles across the semispans of the horizontal tail $\Delta\epsilon$ for the model with the single-rotating propeller and for the model with the dual-rotating propellers. The values of $\Delta\epsilon$ are plotted as a function of thrust coefficient at various propeller blade angles and lift coefficients for the flaps-retracted condition. For the model with the dual-rotating propellers, the difference of downwash across the semispans of the horizontal tail was small; whereas, for the model with the single-rotating propeller, a difference of 8.7° at $T_c = 0.31$ was measured. The large differences of downwash measured across the semispans of the tail of the model with the single-rotating propeller will result in asymmetrical tail loadings and bending moments that may be critical from structural considerations.

For the single-rotating propeller, an asymmetrical dynamic-pressure distribution also exists at the tail because the thrust distribution is not symmetrical at the propeller disk. This dissymmetry of thrust arises from the inclination of the propeller axis to the air stream, which causes both the local relative airspeed and the local angle of attack to be higher on the side of the downgoing blades than on the side of the upgoing blades.

The result is that, as the angle of attack is increased, there is a progressively higher concentration of thrust on the side of the downgoing blades than on the side of the upgoing blades. As an example, with flaps retracted, a difference of $(q/q_o)_{av}$ across the two semispans of the horizontal tail surface of 0.45 at $T_c = 0.31$ was measured (reference 1).

As noted previously (table I), for the model with dual-rotating propellers, the differences of $(q/q_o)_{av}$ across the two semispans of the horizontal tail surface were small.

CONCLUDING REMARKS

The surveys at the tail of the model with dual-rotating propellers showed little evidence of slipstream rotation or asymmetric thrust distribution. The effects of slipstream rotation and asymmetric thrust distribution on the resultant air flow at the tail of the model with the single-rotating propeller, however, were large at high thrust coefficients and at high angles of attack. As a typical example, for the model with dual-rotating propellers and with flaps retracted, the differences of downwash and dynamic pressure across the semispans of the horizontal tail were negligible; whereas, for the model with the single-rotating propeller, differences of downwash and average dynamic-pressure ratio of 8.7° and 0.45, respectively, were measured across the elevator hinge line at a thrust coefficient of 0.31.

Langley Memorial Aeronautical Laboratory,
National Advisory Committee for Aeronautics,
Langley Field, Va.

REFERENCES

1. Pass, H. R.: Wind-Tunnel Study of the Effects of Propeller Operation and Flap Deflection on the Pitching Moments and Elevator Hinge Moments of a Single-Engine Pursuit-Type Airplane. NACA A.R.R., July 1942.

2. Sweberg, Harold H.: The Effect of Propeller Operation on the Air Flow in the Region of the Tail Plane for a Twin-Engine Tractor Monoplane. NACA A.R.R., Aug. 1942.

3. DeFrance, Smith J.: The N.A.C.A. Full-Scale Wind Tunnel. Rep. No. 459, NACA, 1933.

4. Silverstein, Abe, and Katzoff, S.: Experimental Investigation of Wind-Tunnel Interference on the Downwash behind an Airfoil. Rep. No. 609, NACA, 1937.

5. Theodorsen, Theodore, and Silverstein, Abe: Experimental Verification of the Theory of Wind-Tunnel Boundary Interference. Rep. No. 478, NACA, 1934.

TABLE I

AVERAGE DYNAMIC-PRESSURE RATIOS AND AVERAGE DOWNWASH ANGLES AT TAIL OF MODEL WITH DUAL-ROTATING PROPELLERS

α_T (deg)	C_L	δ_f (deg)	T_c	$(q/q_o)_{av}$		ϵ_{av} (deg)	
				Right semispan of tail	Left semispan of tail	Right semispan of tail	Left semispan of tail
−0.7	0.130	0	(1)	0.99	0.97	1.7	1.9
3.7	.407	0	(1)	.98	.97	2.5	2.7
8.1	.723	0	(1)	.94	.95	5.8	5.8
7.1	1.275	40	(1)	.95	.95	11.9	12.3
11.5	1.565	40	(1)	.93	.93	13.9	13.5
−.7	.102	0	0.025	1.02	1.00	1.4	1.7
−.7	.125	0	.250	1.24	1.21	1.3	1.5
3.7	.435	0	.025	1.00	1.00	2.9	3.3
3.7	.450	0	.250	1.19	1.19	3.2	3.6
7.0	1.396	40	.300	1.07	1.31	14.7	13.2
6.8	1.532	40	.600	1.17	1.43	17.4	14.4
11.3	1.772	40	.300	1.24	1.25	18.7	17.2
11.3	1.815	40	.600	1.33	1.44	21.7	19.2

[1]Propellers removed.

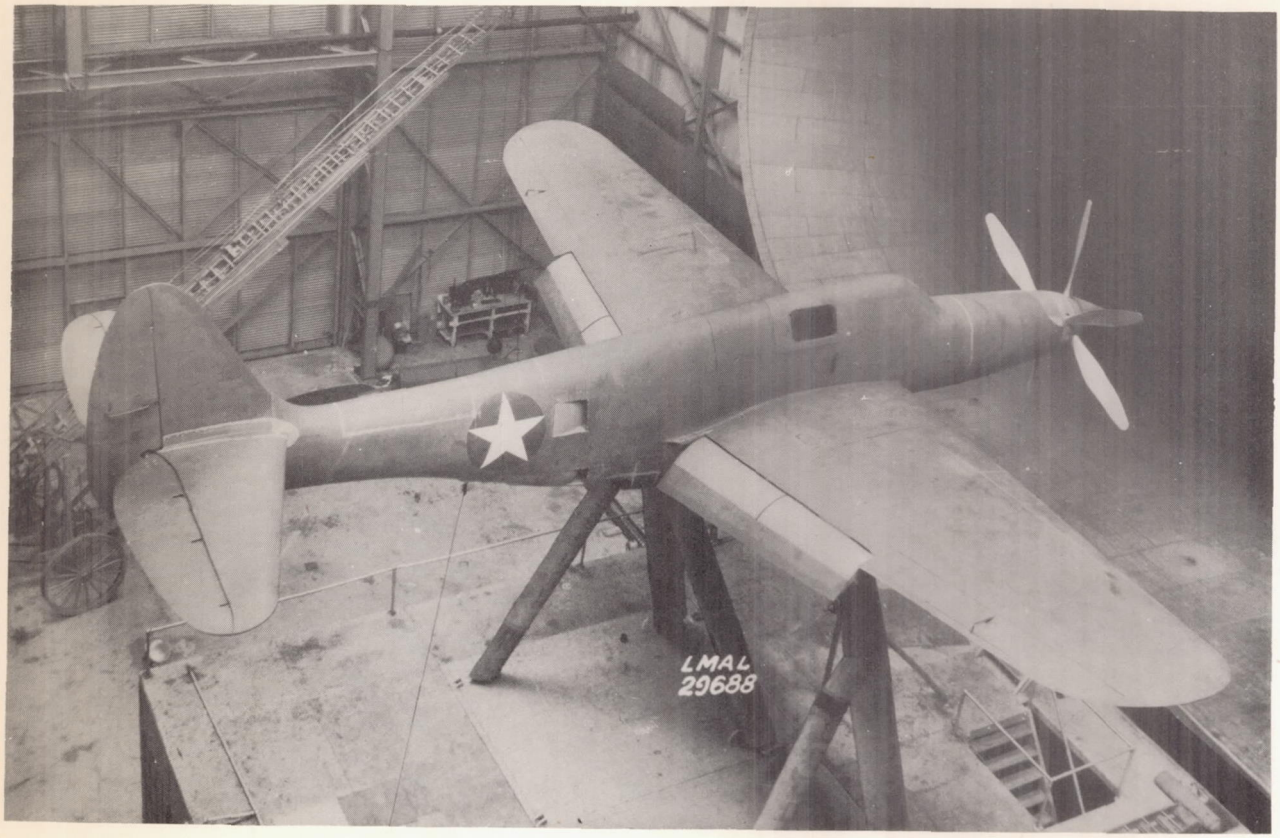

Figure 1.- Model mounted in the NACA full-scale tunnel.

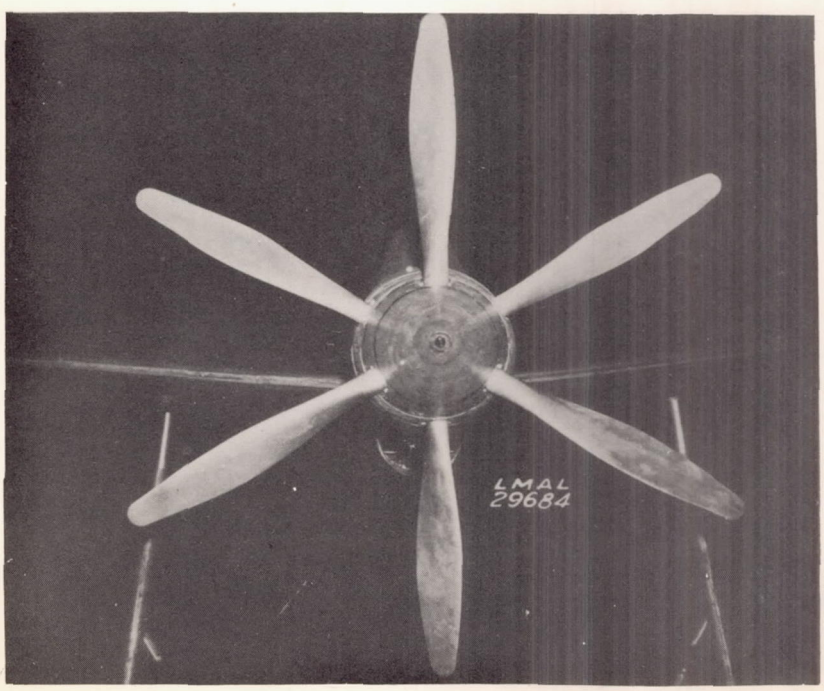

Figure 3.- Propeller installation on model

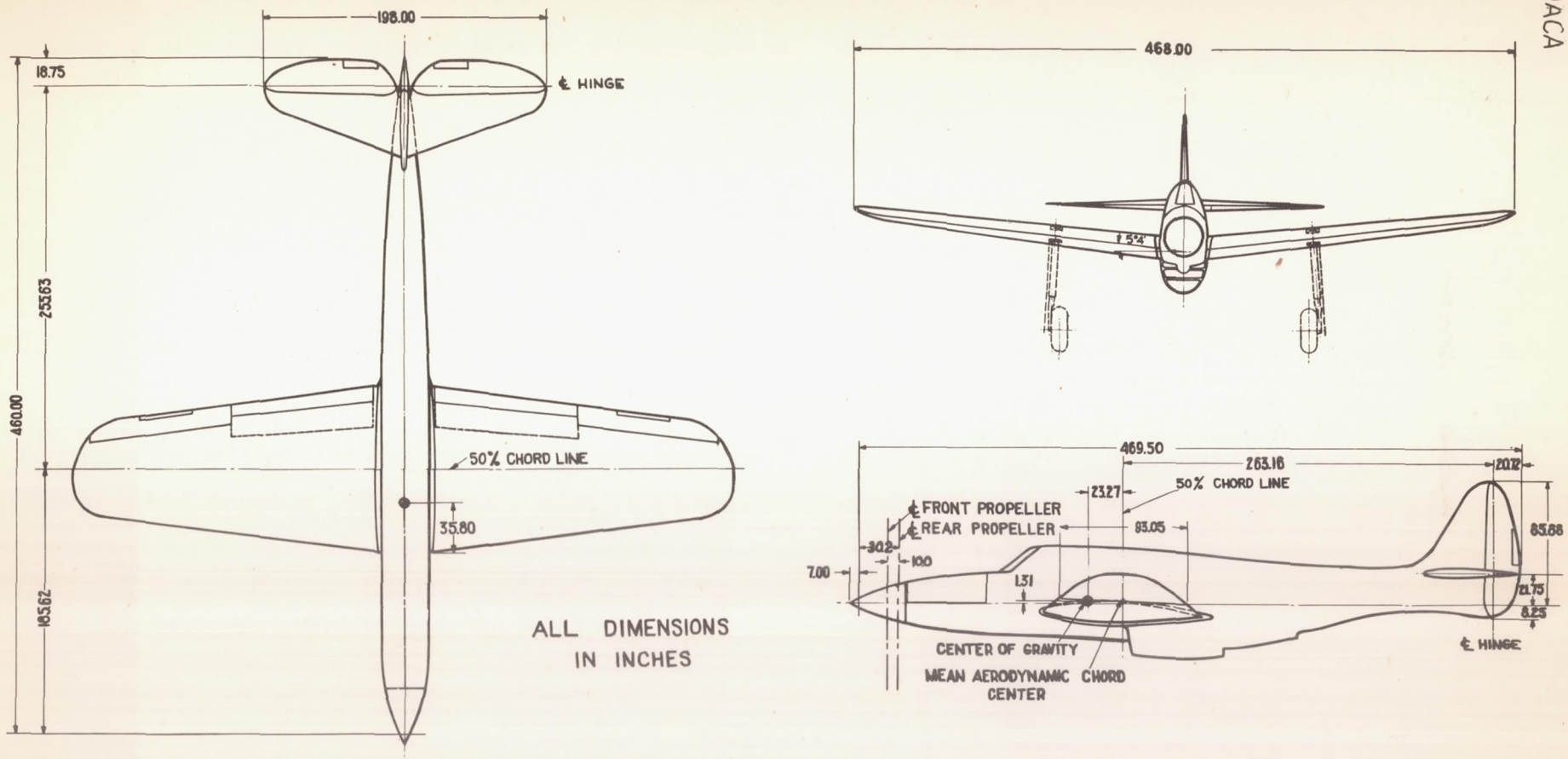

FIGURE 2.- THREE-VIEW DRAWING OF MODEL.

NACA

Fig. 2

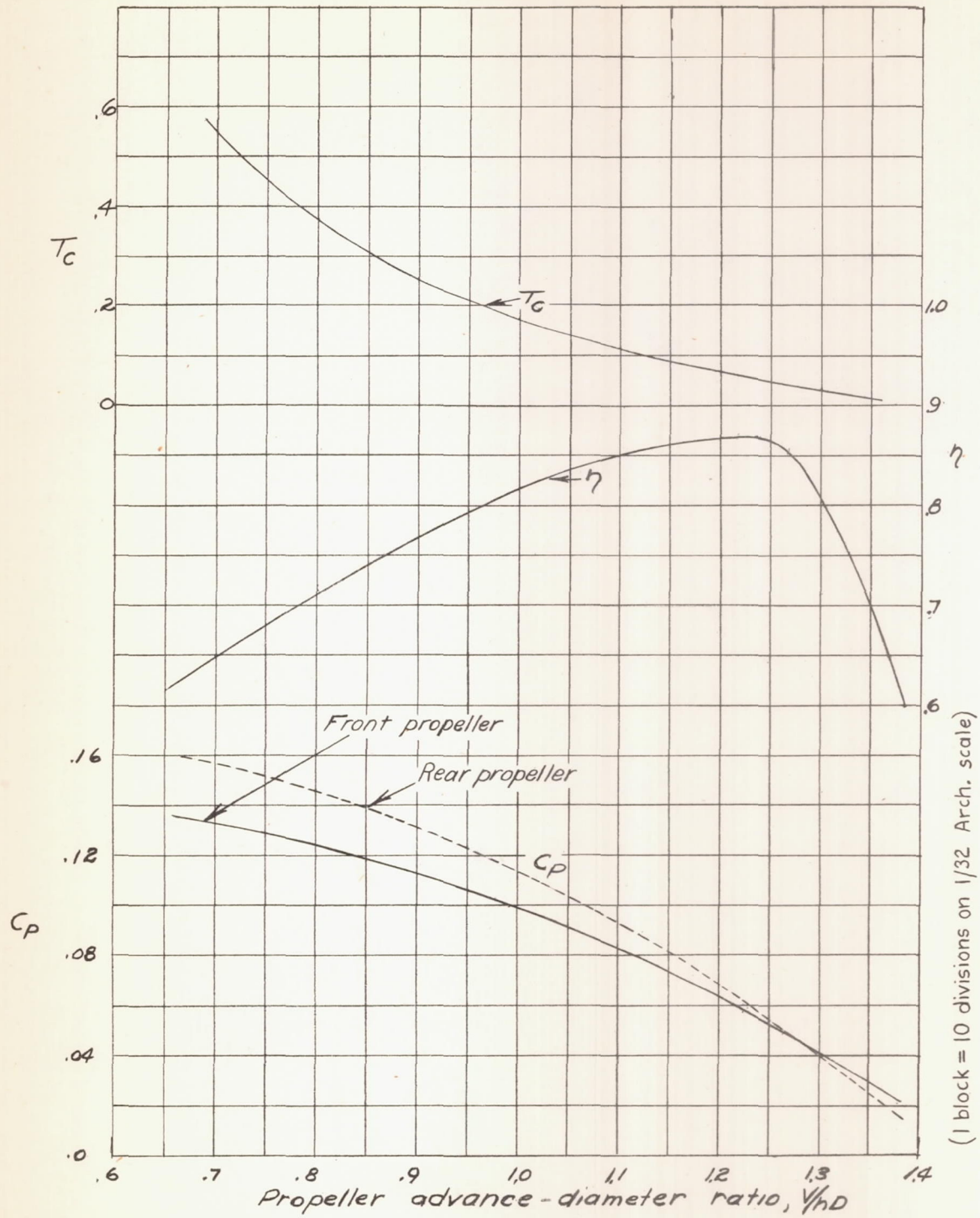

Figure 4.-Propeller characteristics as determined from tests of complete model in the NACA full-scale tunnel. Six-blade dual-rotating propeller; propeller diameter 10 feet; β_F, 28.0°; β_R, 27.7°.

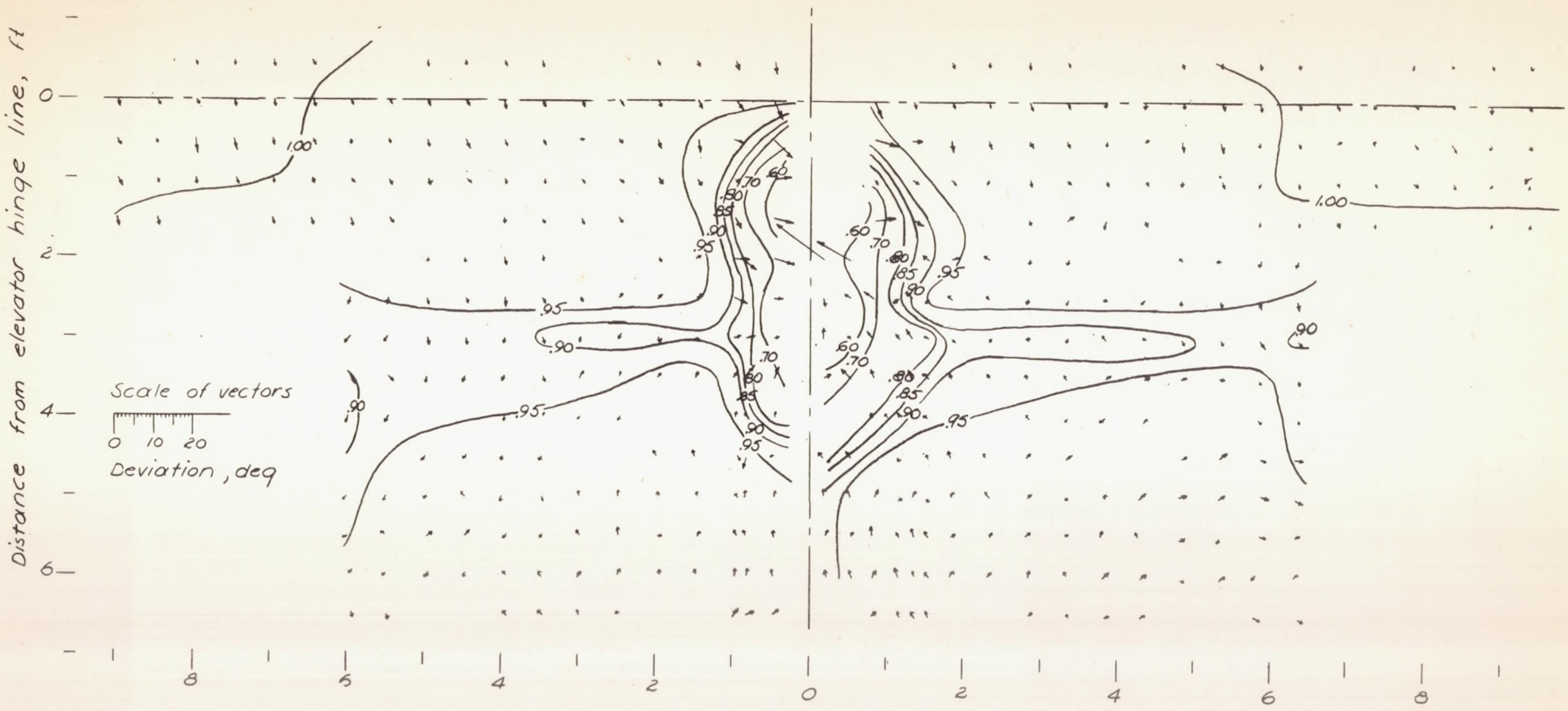

(a) $\alpha_r = -0.7°$.

Figure 5.- Dynamic-pressure (q/q_0) contours and inclination of the air stream in the plane of the elevator hinge line. Vectors show angular deviation of air flow from free-stream direction. View looking forward. Propellers removed; flaps retracted; horizontal and vertical tail surfaces removed.

NACA

Fig. 5a

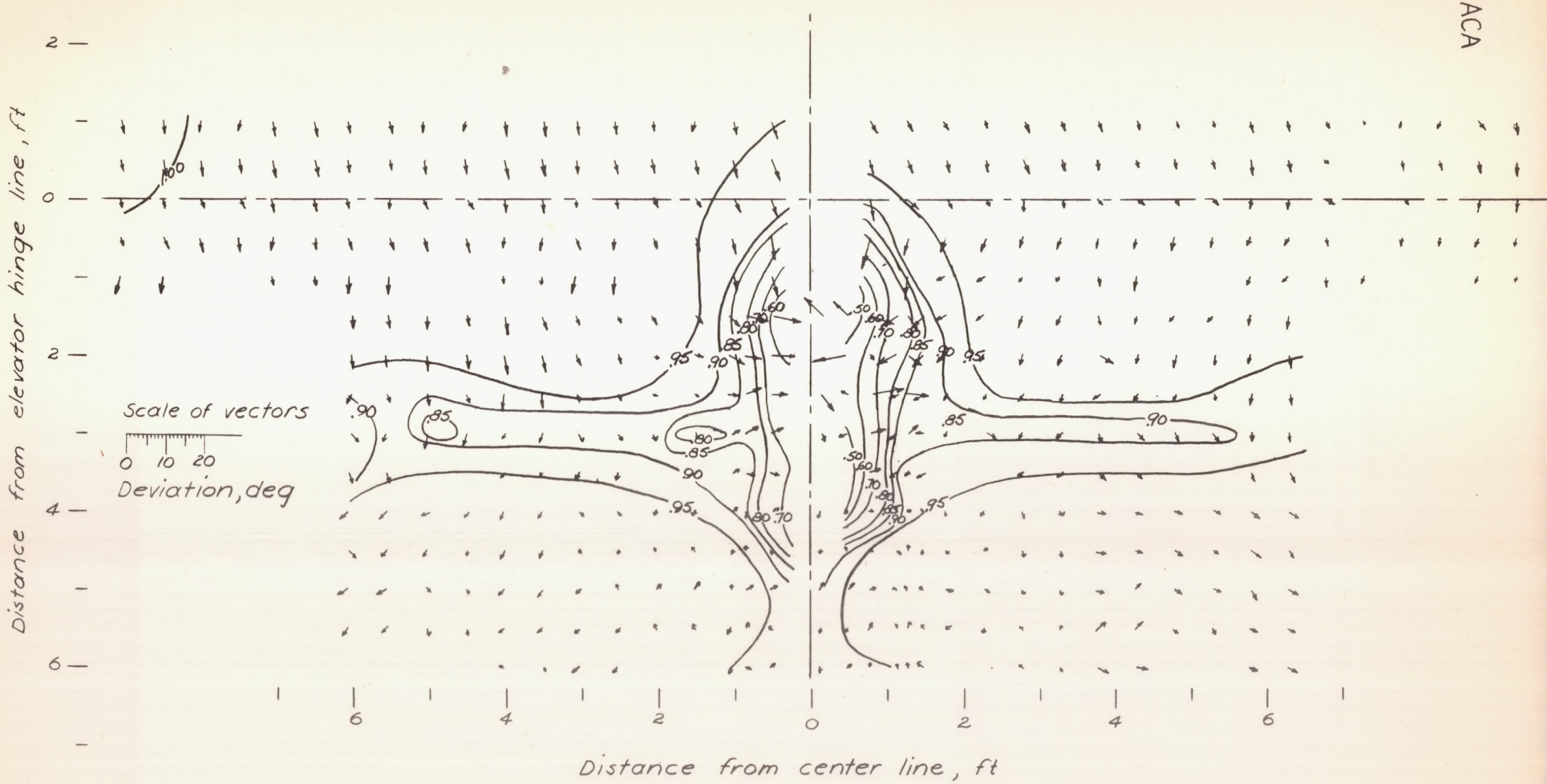

(b) $\alpha_T = 3.7°$

Figure 5.- Continued.

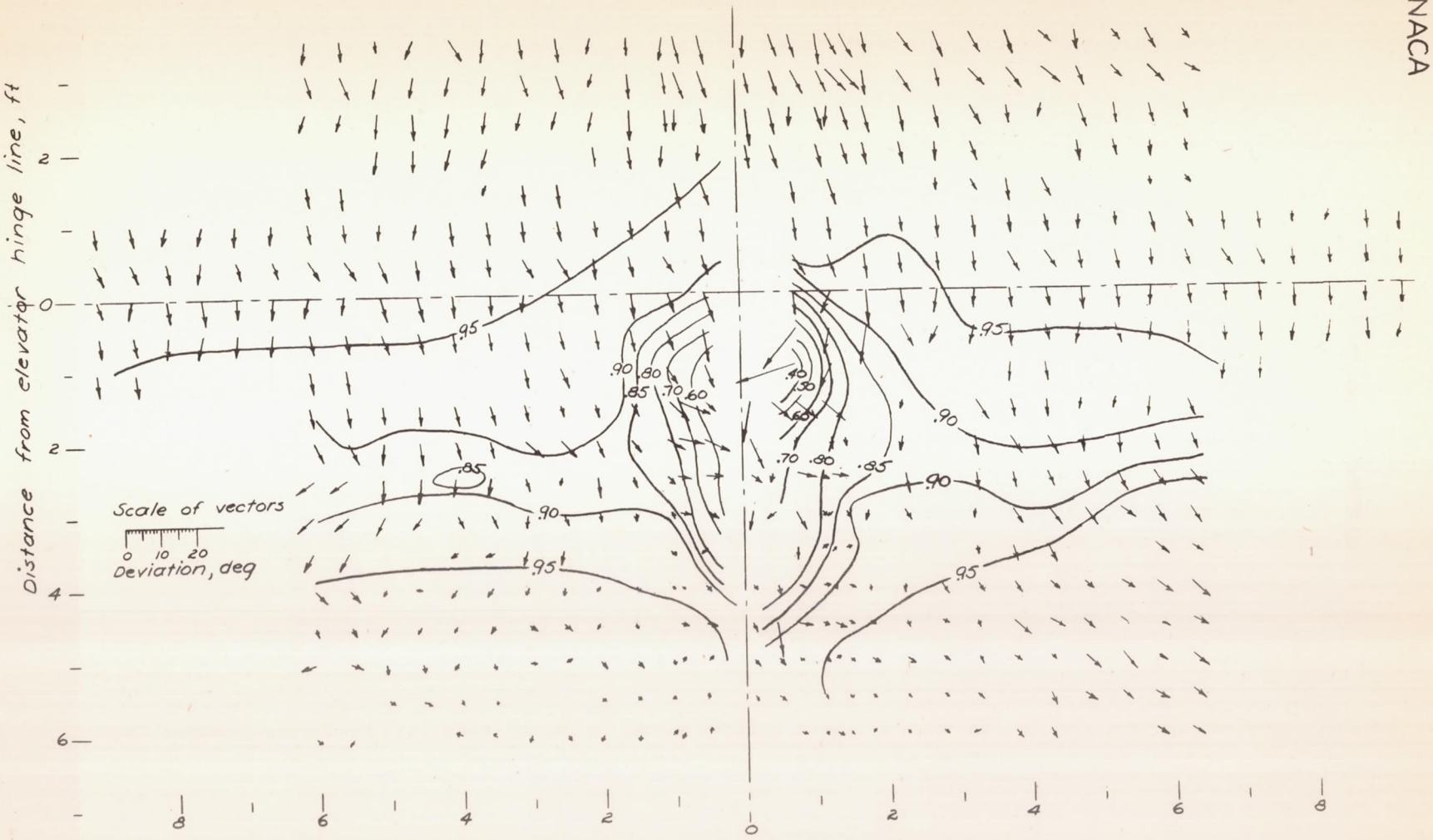

(c) $\alpha_T = 8.1°$.

Figure 5. - Concluded.

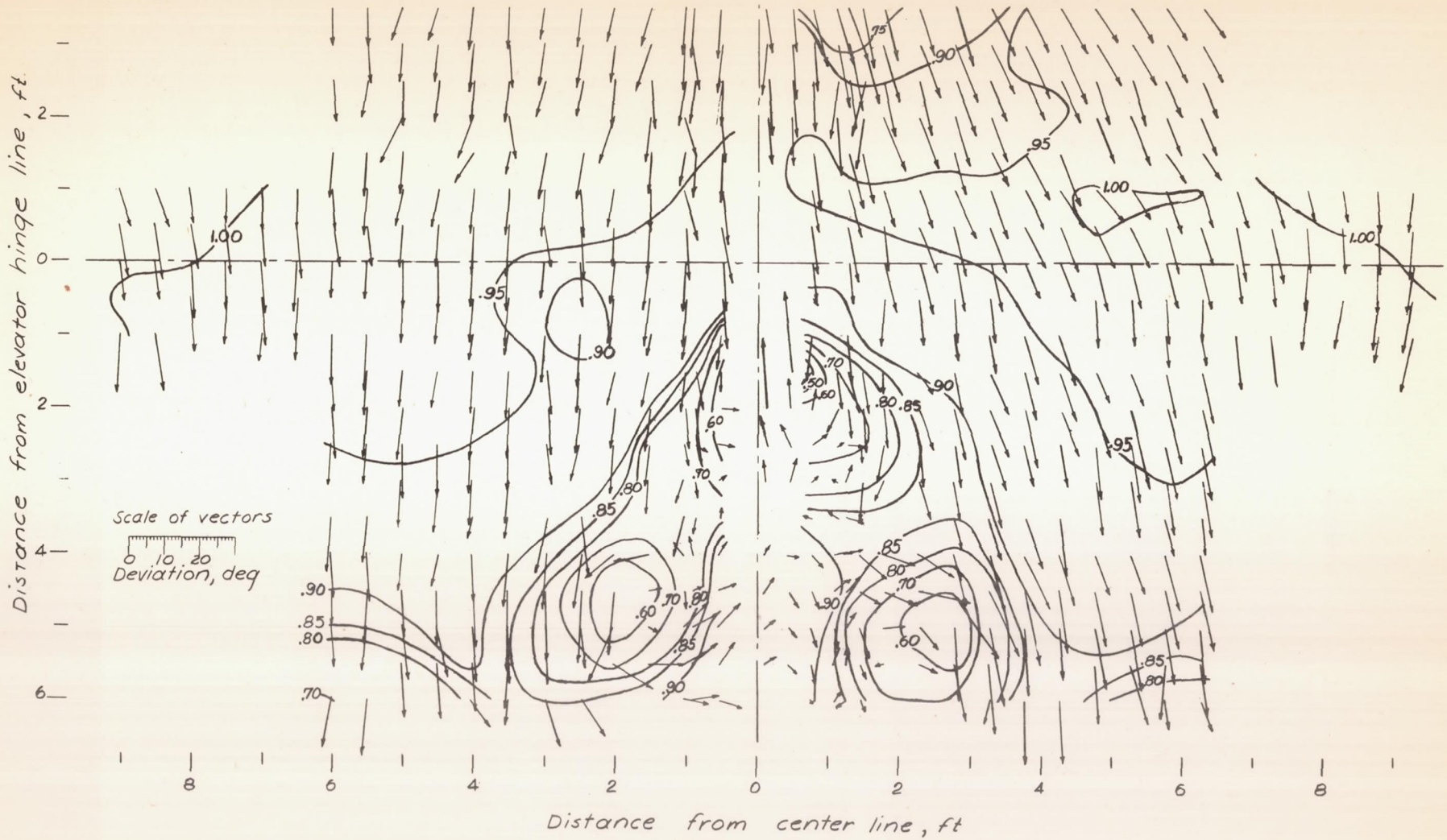

(a) $\alpha_T = 7.1°$

Figure 6.- Dynamic-pressure (q/q_0) contours and inclination of the air stream in the plane of the elevator hinge line. Vectors show angular deviation of air flow from free-stream direction. View looking forward. Propellers removed; flaps deflected 40°; horizontal and vertical tail surfaces removed.

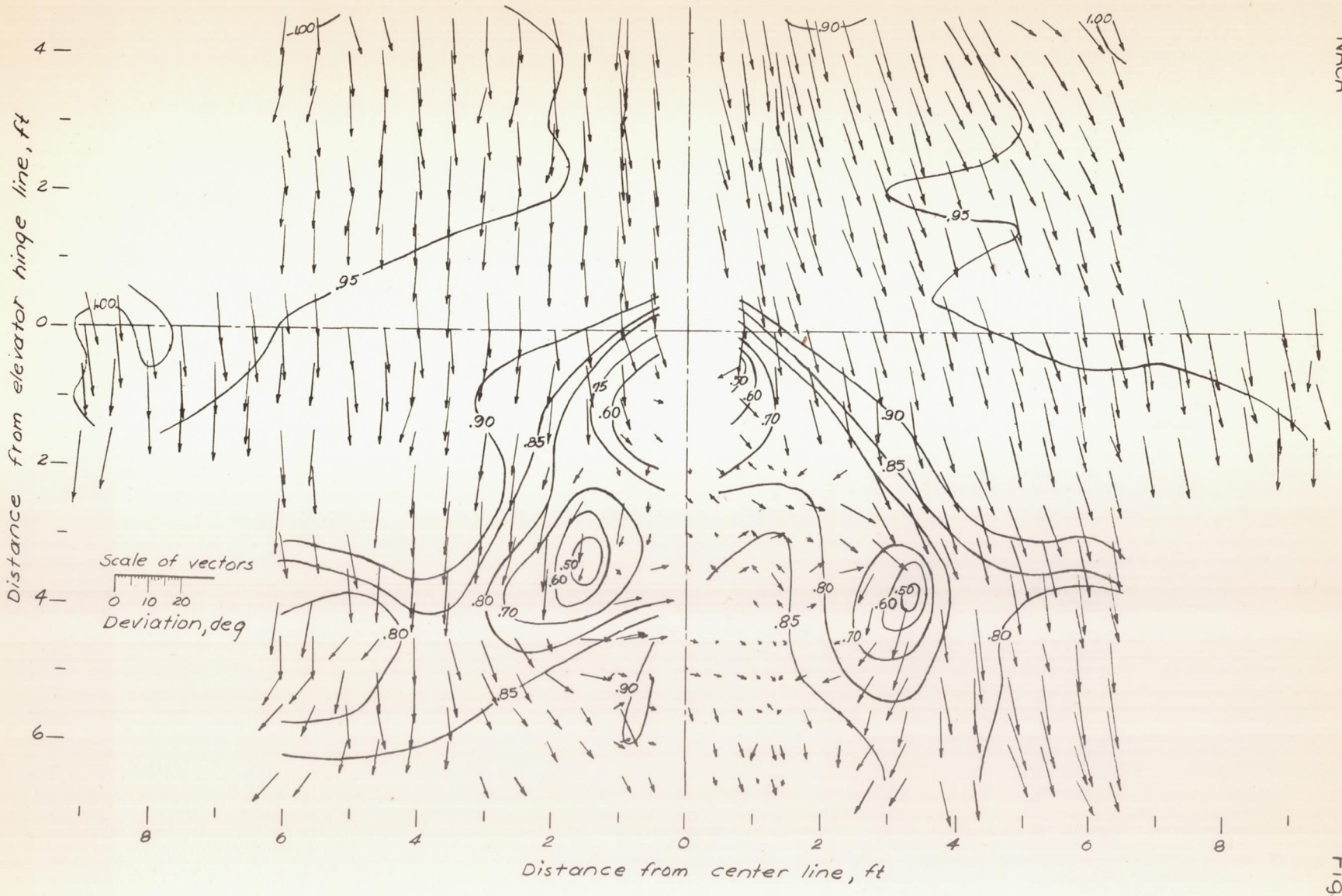

(b) $\alpha_T = 11.5°$.

Figure 6.- Concluded.

NACA

Fig. 6b

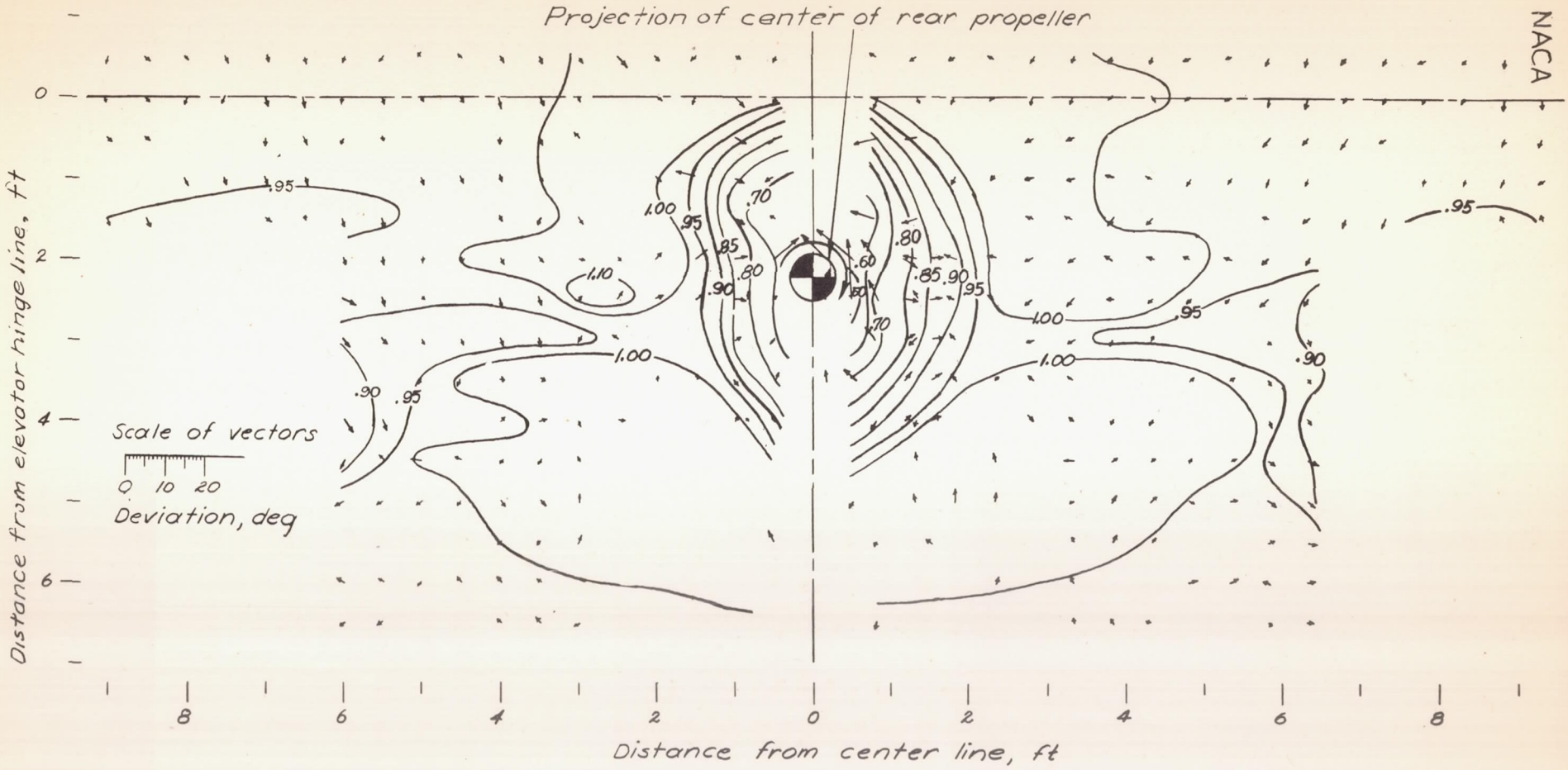

(a) $\alpha_T = -0.7°$; $T_c = 0.025$.

Figure 7. - Dynamic-pressure (q/q_o) contours and inclination of the air stream in the plane of the elevator hinge line. Vectors show angular deviation of air flow from free-stream direction. View looking forward. Propellers operating; flaps retracted; vertical and horizontal tail surfaces removed.

Fig. 7a

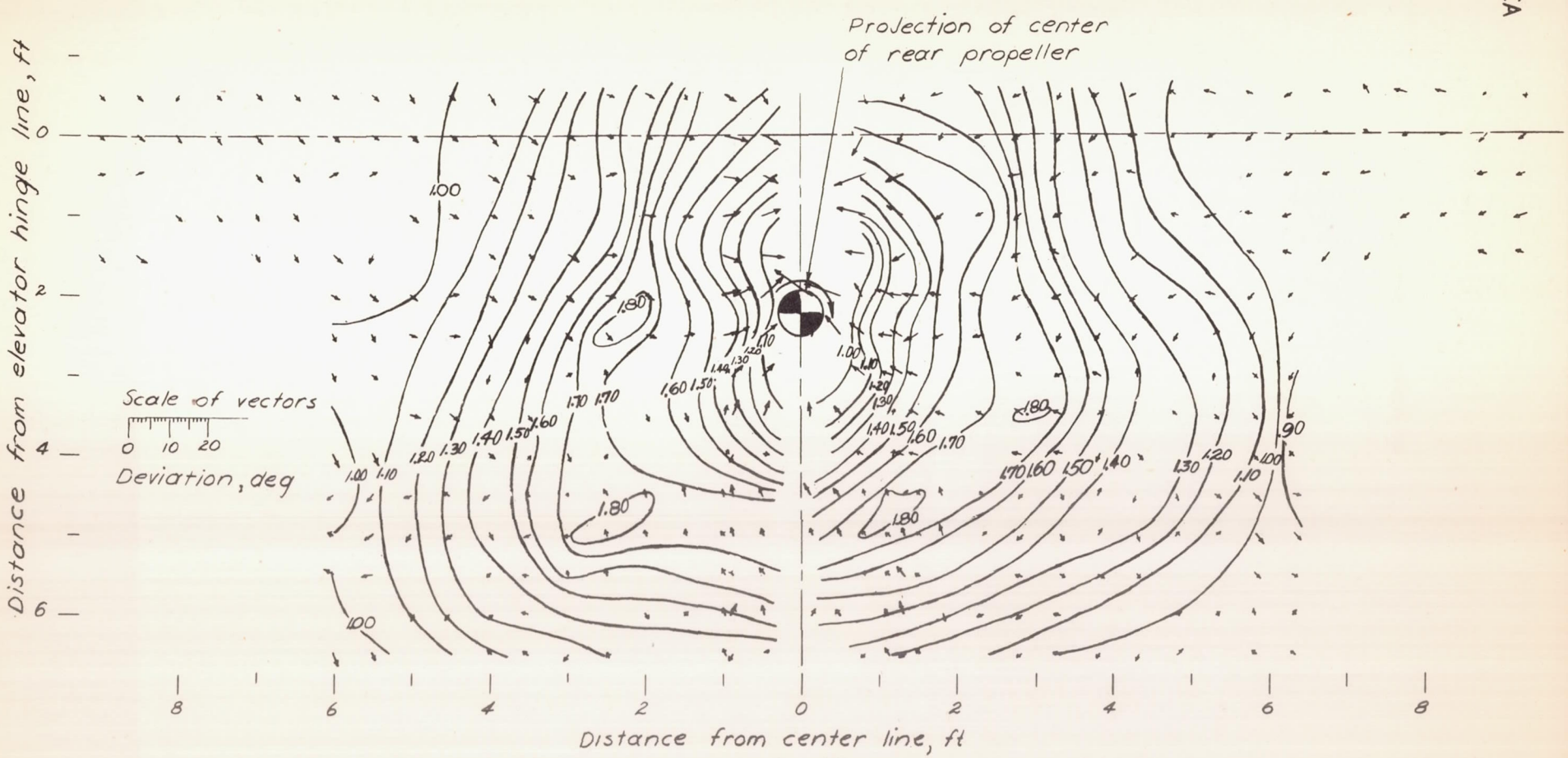

(b) $\alpha_T = -0.7°$; $T_c = 0.25$.

Figure 7. - Continued.

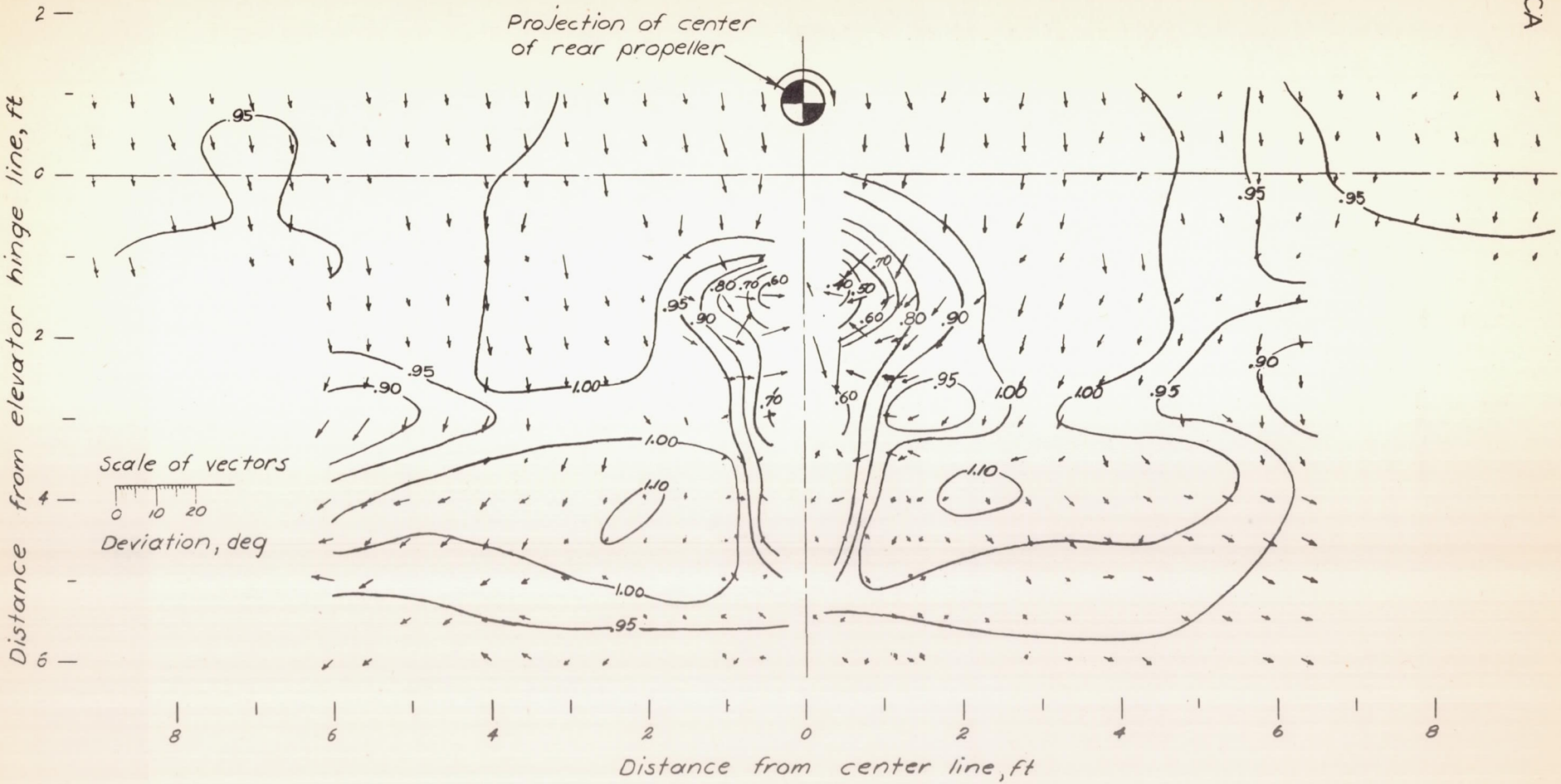

(c) $\alpha_T = 3.7°$; $T_C = 0.025$.

Figure 7.- Continued.

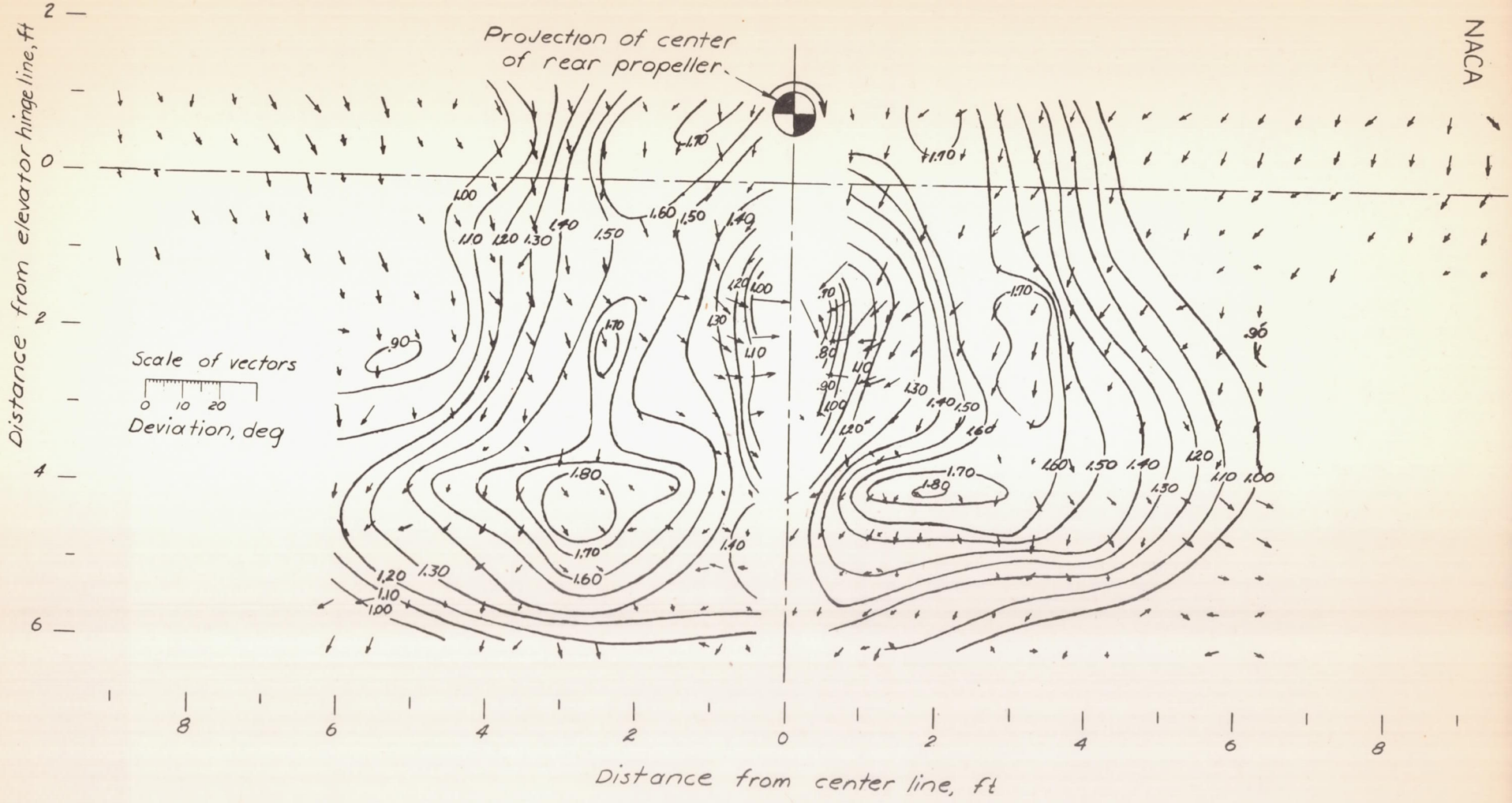

(d) $\alpha_T = 3.7°$; $T_C = 0.25$.

Figure 7. - Concluded.

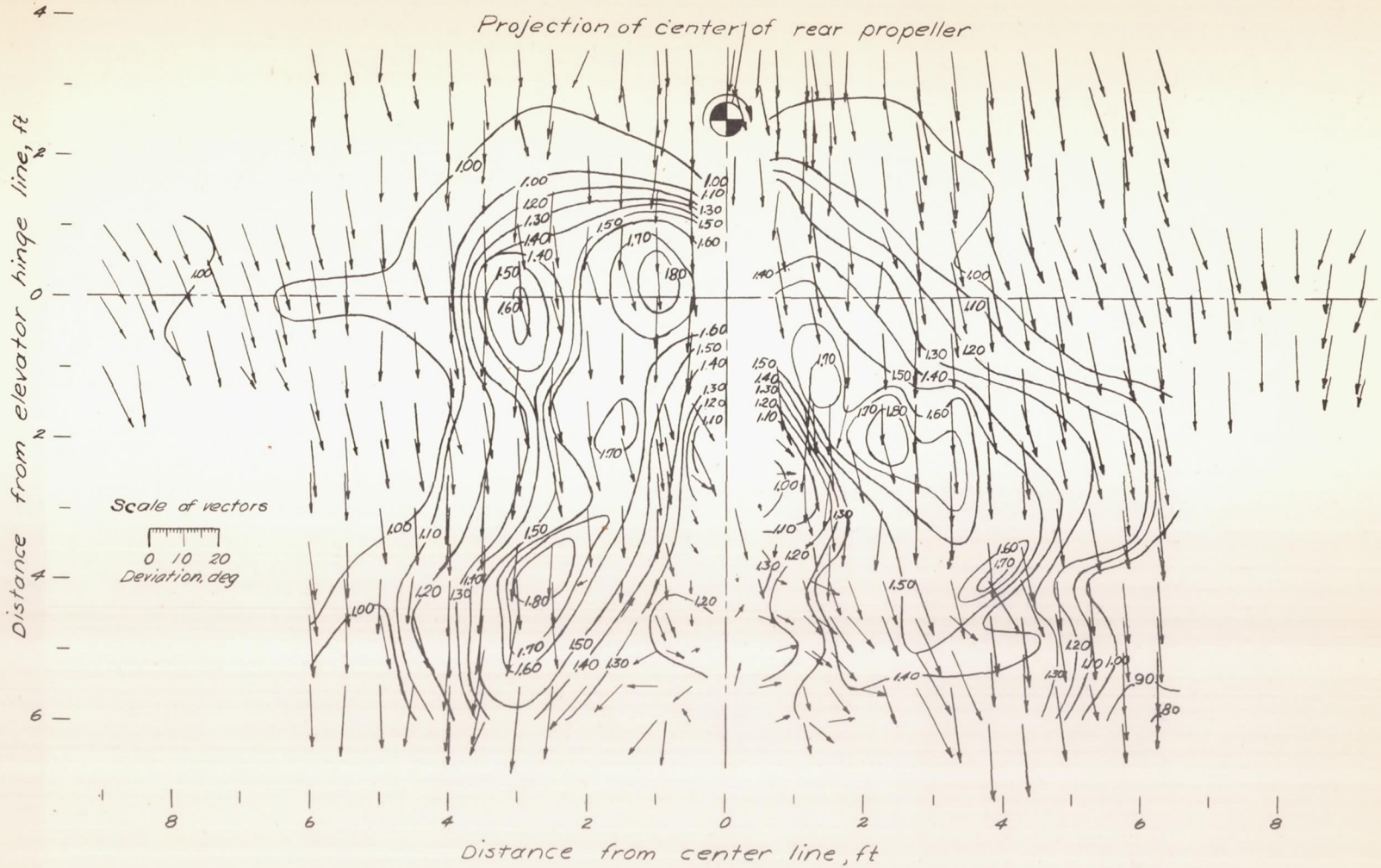

(a) $\alpha_T = 7.0°$; $T_C = 0.300$.

Figure 8.- Dynamic-pressure (q/q_0) contours and inclination of the air stream in the plane of the elevator hinge line. Vectors show angular deviation of air flow from free-stream direction. View looking forward. Propellers operating; flaps deflected 40°; horizontal and vertical tail surfaces removed.

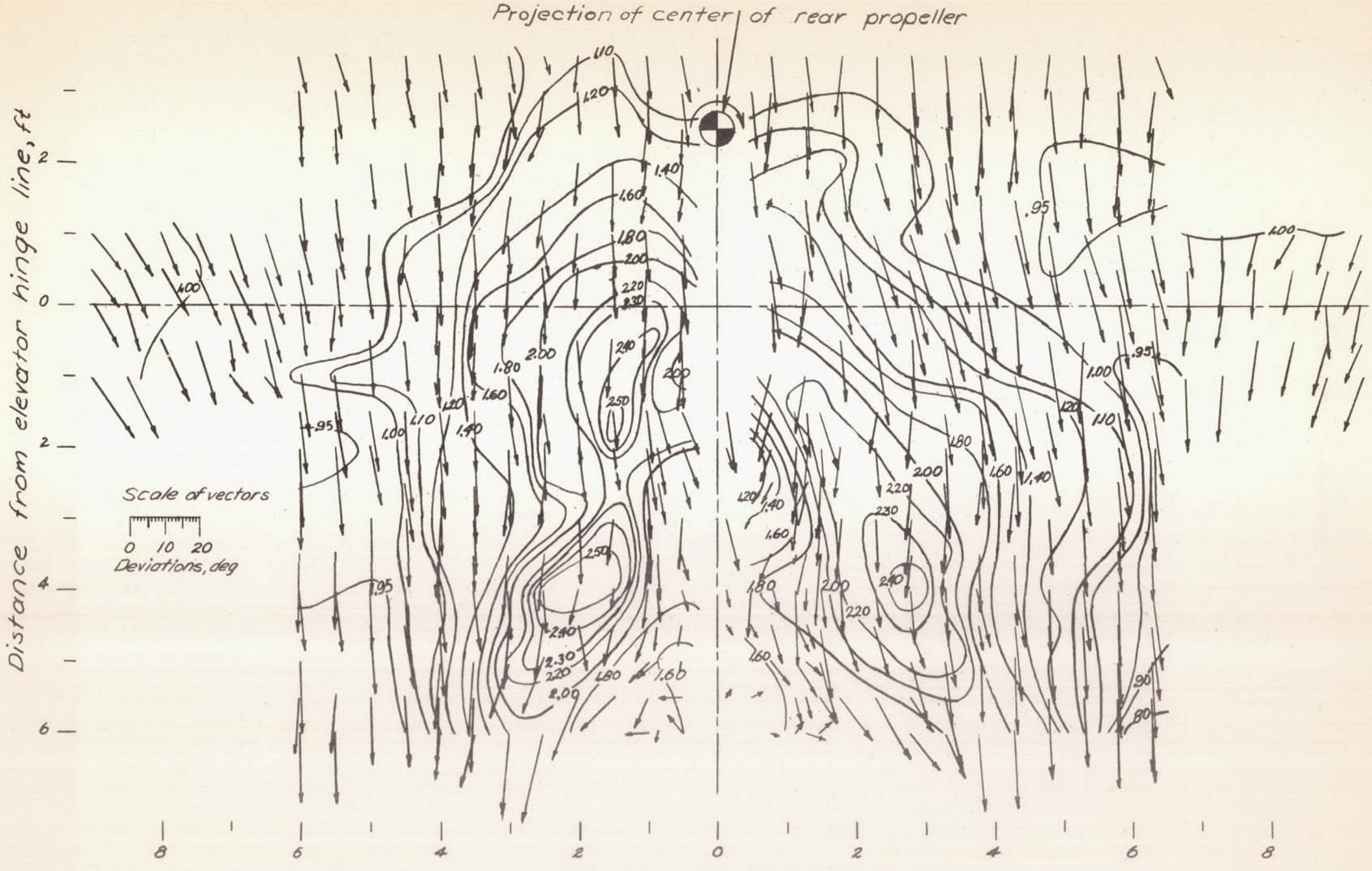

(b) $\alpha_T = 6.8°$; $T_C = 0.600$.

Figure 8. - Continued.

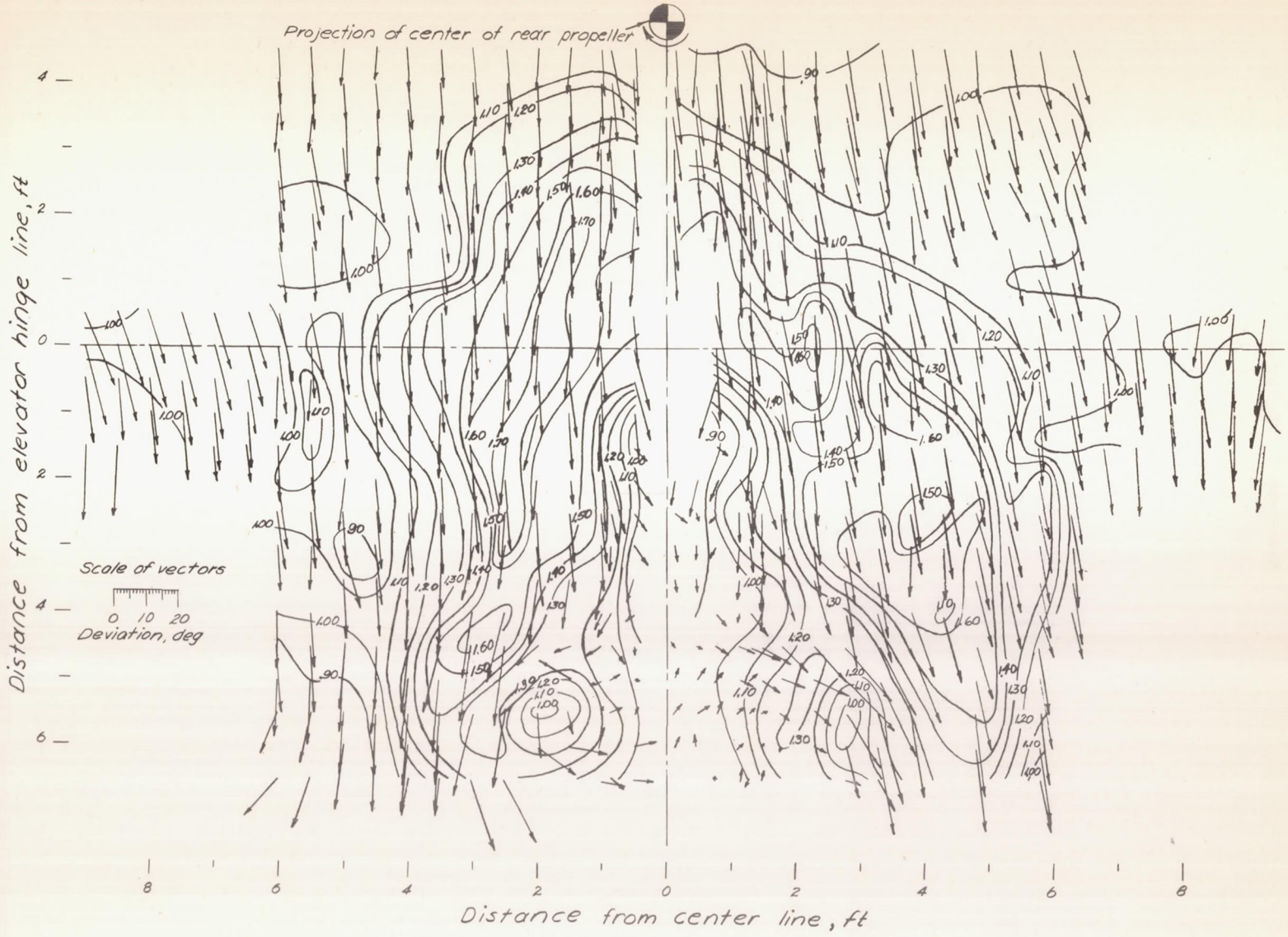

(c) $\alpha_T = 11.3°$; $T_C = 0.300$.

Figure 8.- Continued.

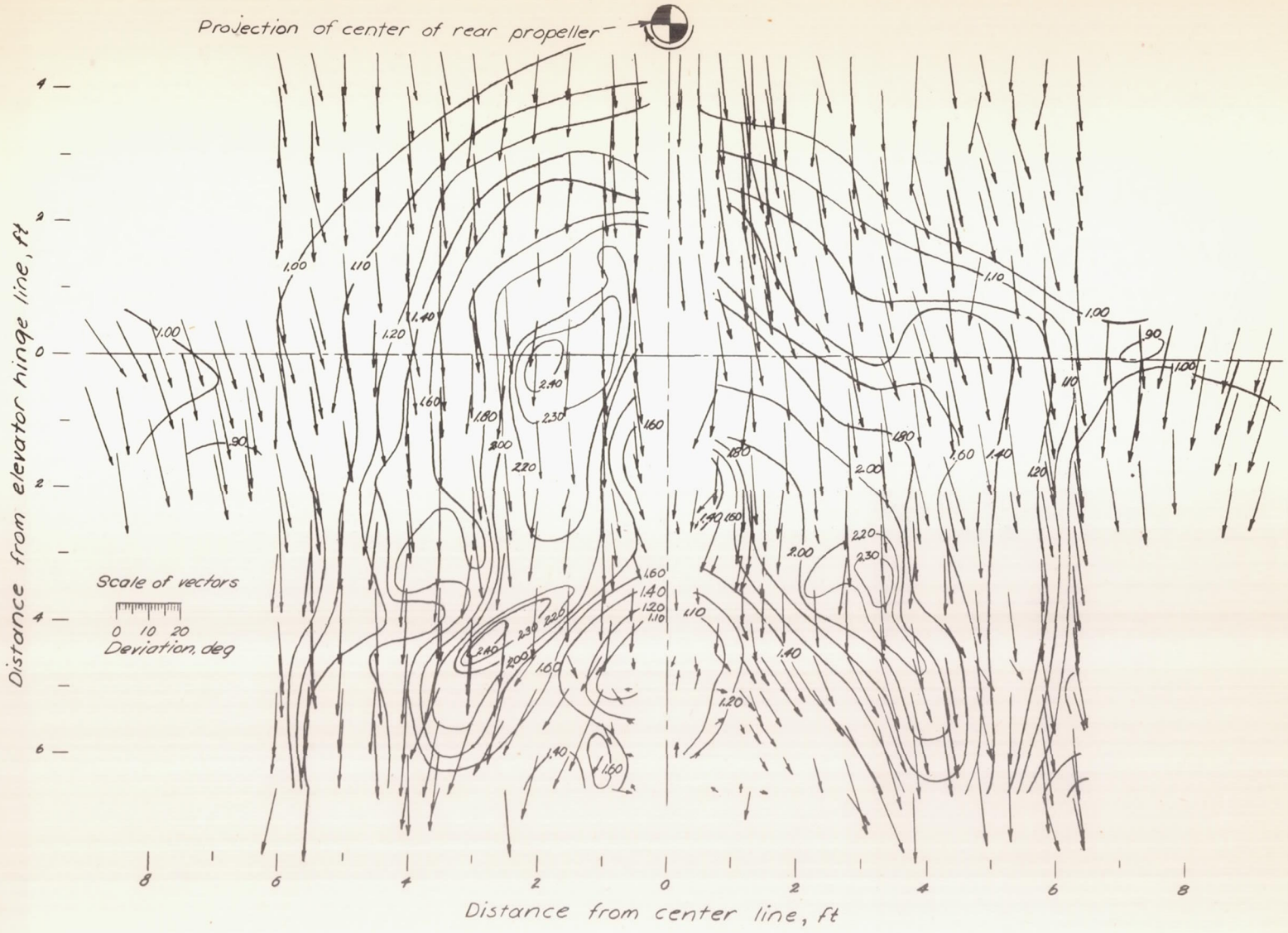

(d) $\alpha_T = 11.3°$; $T_c = 0.600$.

Figure 8.- Concluded.

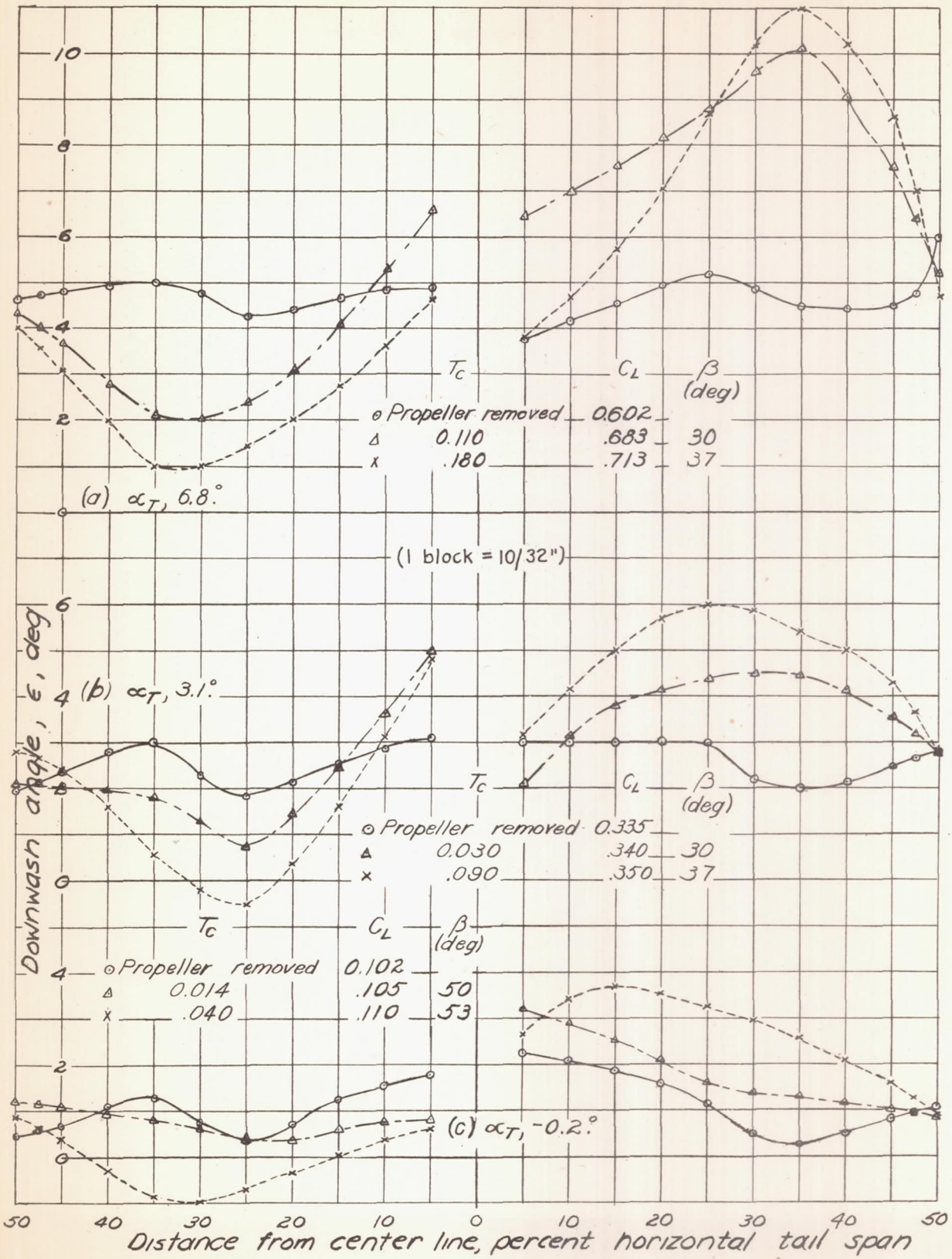

Figure 9.- Variation of downwash angle across the horizontal tail span of model equipped with single-rotating propeller. Values from reference 1. Flaps retracted.

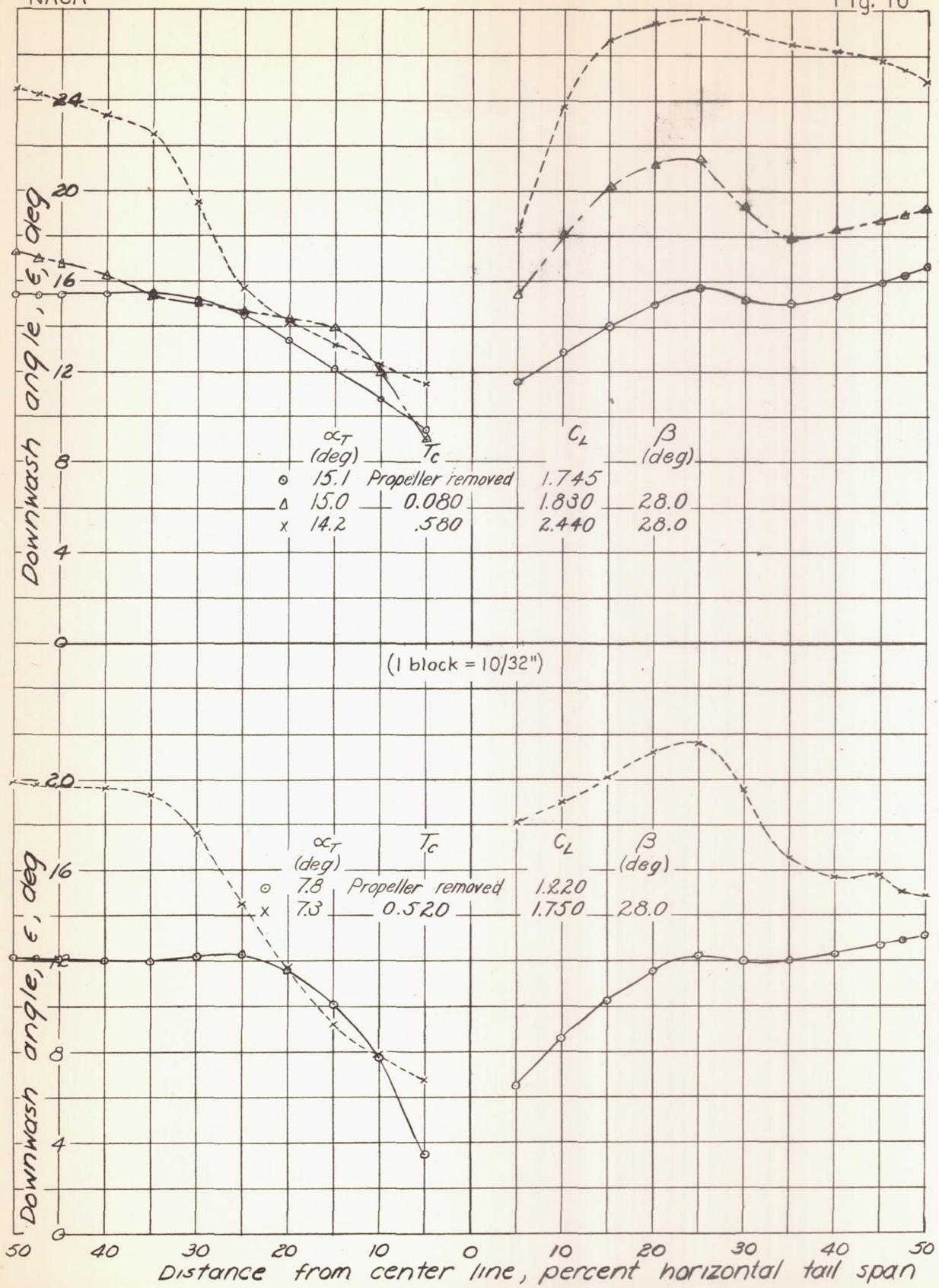

Figure 10.- Variation of downwash angle across the horizontal tail span of model equipped with single-rotating propeller. Values from reference 1. Flaps deflected 40.

(1 block = 10/32")

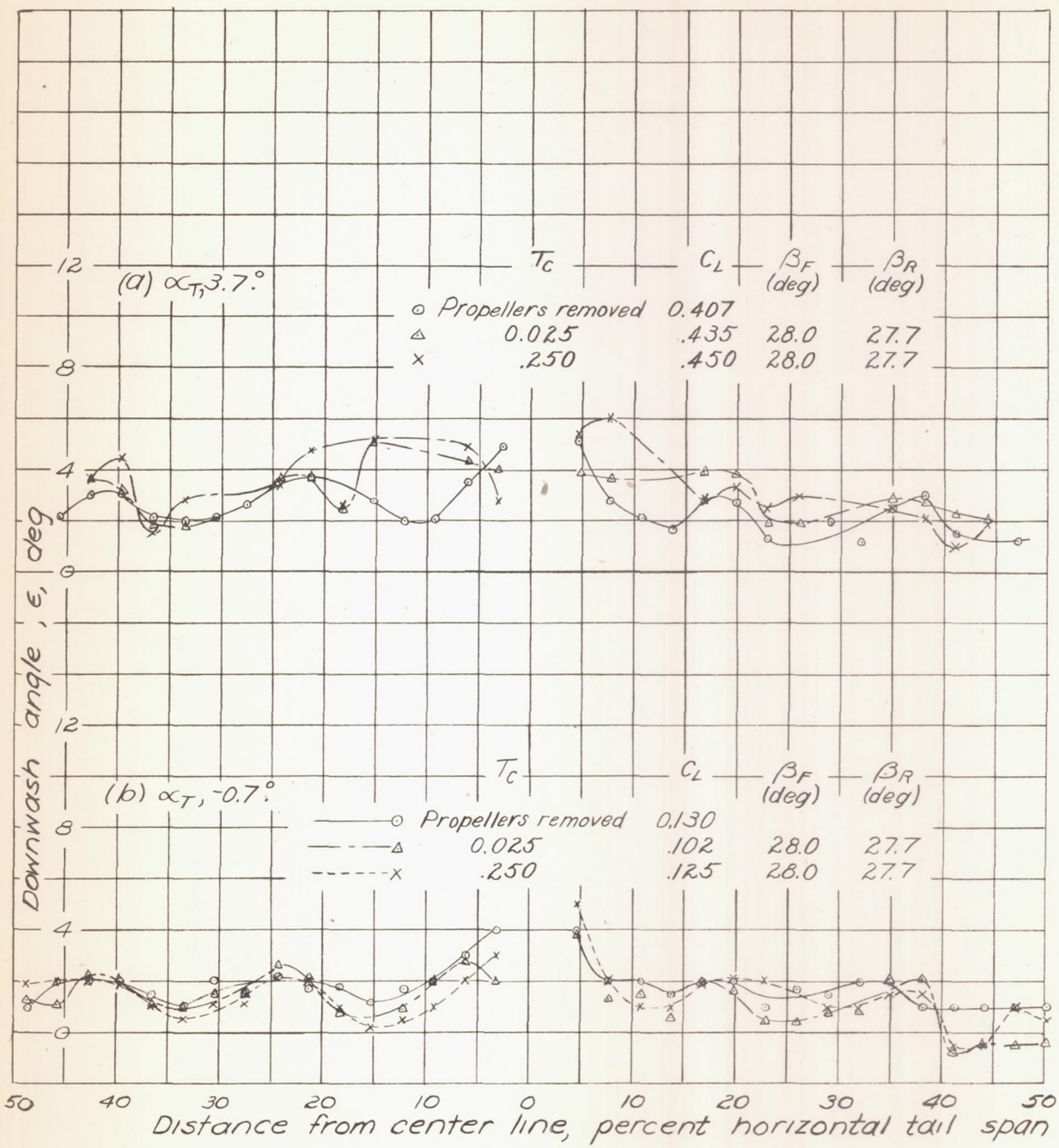

Figure 11.- Variation of downwash angle across the horizontal tail span of model equipped with dual-rotating propellers. Flaps retracted.

NACA

(1 block = 10/32")

Fig. 12

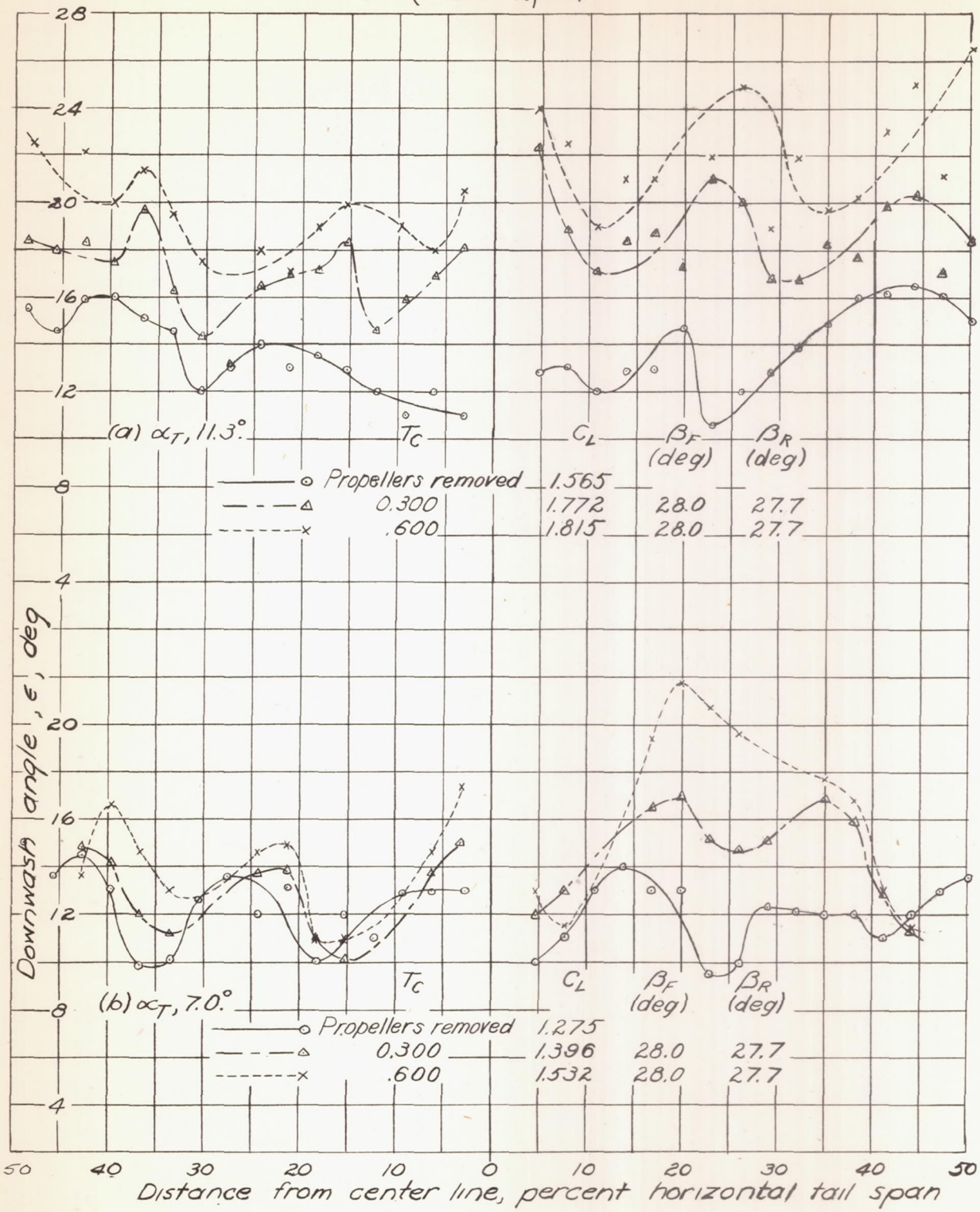

Figure 12.- Variation of downwash angle across the horizontal tail span of model equipped with dual-rotating propellers. Flaps deflected 40°.

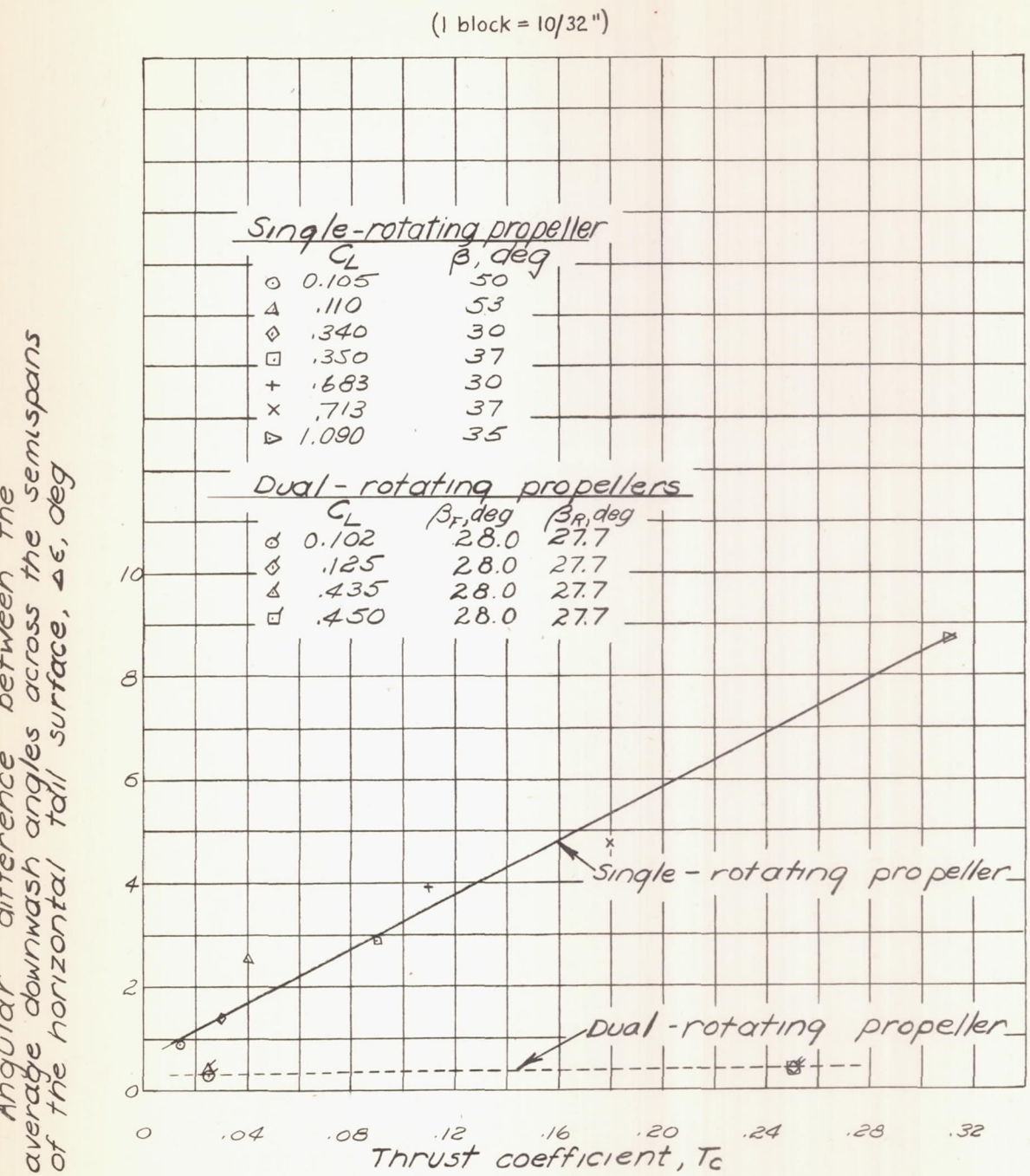

Figure 13.- Comparison of downwash differences across semispans of the horizontal tail surfaces of the model with single-rotating propeller and model with dual-rotating propellers. Flaps retracted.